Electronic Supplementary Information

Facile Synthesis of Mixed Phase 1T/2H-MoS_2 Heterostructured Nanosheets with Highly Efficient Solar Light-Driven Photocatalyst and Recyclable Adsorbent

Sahil Thakur[a], Ayush Badoni[a], Samriti[a,b], A. Savoyant[c], Swart Hendrik Christoffel[d], Mikhael Bechelany[e,f], Andrej Kuznetsov[b], Jai Prakash[a]*

[a]Department of Chemistry, National Institute of Technology Hamirpur, Hamirpur (H.P.)-177005, India

[b]Department of Physics and Centre for Materials Science and Nanotechnology, University of Oslo, Oslo N-0316, Norway

[c]Aix-Marseille Université, CNRS, Université de Toulon, IM2NP (UM3 7334), Marseille, France.

[d]Department of Physics, University of the Free State (UFS), Bloemfontein, ZA 9300, South Africa

[e]Institut Européen des Membranes, IEM, UMR-5635, University Montpellier, ENSCM, CNRS, Place Eugene Bataillon, 34095 Montpellier, France

[f]Functional Materials Group, Gulf University for Science and Technology, Mubarak Al-Abdullah, 32093, Kuwait

***Corresponding author:**

Jai Prakash (Email: jaip@nith.ac.in)

Table of Contents

1. Experimental Section

1.1 Materials

Molybdenum trioxide (MoO_3) (99%, Ottokemi), Thiourea ($SC(NH_2)_2$) (99% Fisher Scientific), L-cysteine ($C_3H_7NO_2S$) (98.5% Loba Chemicals), Thioacetamide (C_2H_5NS) (98% Tokyo Chemical Industry) were used for the preparation of MoS_2 samples.

1.2 Synthesis of MoS_2

The MoS_2 samples were synthesized via a hydrothermal method using three distinct organic sulfur precursors, each with different sulfur ion release rates, as illustrated in **Scheme S1**. For each sample, MoO_3 and the respective sulfur precursor (thioacetamide, L-cysteine, or thiourea) were weighed in stoichiometric ratios and dissolved in 70 mL of deionized water. The mixture was continuously stirred for 40 minutes to ensure proper dissolution and mixing. Subsequently, the solution was transferred to an 80 mL Teflon-lined stainless-steel autoclave and subjected to hydrothermal treatment at 180°C for 24 hours. After the reaction period, the autoclave was allowed to cool naturally to room temperature. The resulting black products were collected through filtration and purified by alternate washing with distilled water and ethanol. The washed products were then dried in an oven at 60°C for 10 hours. The final products were named as MoS_2-I, MoS_2-II, and MoS_2-III, corresponding to samples prepared using thioacetamide, L-cysteine, and thiourea as sulfur precursors, respectively.

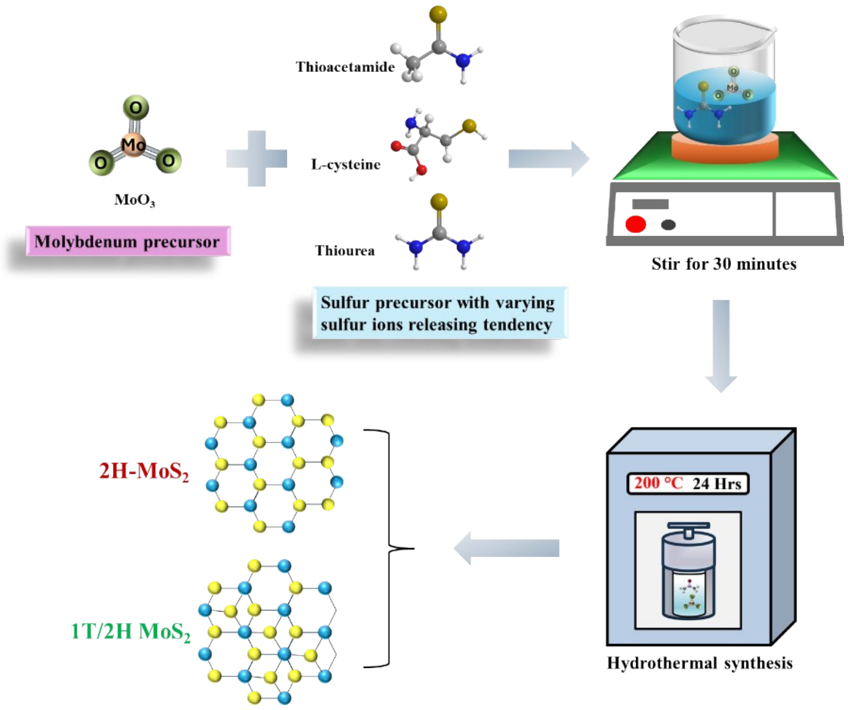

Scheme S1. Schematic illustration of the stepwise synthesis of MoS_2 samples.

1.3 Characterization

The morphological features of MoS_2 samples were characterized using scanning electron microscopy (SEM, EVO18 Carl Zeiss) and high-resolution transmission electron microscopy (HRTEM, Philips CM100). X-ray photoelectron spectroscopy (XPS, PHI 5000 Versaprobe) was used to analyze elemental composition and chemical bonding states. Functional groups were identified using Fourier transform infrared spectroscopy (FTIR, PerkinElmer). Structural characterization was performed using Raman spectroscopy (WiTec, Ar-ion laser $\lambda = 514$ nm) and X-ray diffraction (XRD, Cu Kα radiation, $\lambda = 0.15406$ nm). Surface area and porosity were measured by Brunauer-Emmett-Teller (BET) Autosorb iQ-x analysis under N_2 atmosphere. Thermal stability was evaluated using thermogravimetric analysis (TGA, EXSTAR SII 6300) from 32-700°C. Optical properties were analyzed using UV-visible spectroscopy (UH5300) and photoluminescence spectroscopy (Lambda 45 PerkinElmer at λ_{ex} 532 nm). Electron spin resonance (ESR) was used for the analysis of paramagnetic properties. Electrochemical measurements were conducted using a Metrohm Autolab workstation with a three-electrode system (Pt counter electrode, Ag/AgCl reference electrode, and MoS_2-modified carbon working electrode) in 0.1 M Na_2SO_4 electrolyte.

1.4 Adsorption and Photocatalytic measurements

The photocatalytic experiment was conducted at ambient temperature (25 ± 2°C) by dispersing 10 mg of the photocatalyst in 50 mL of MB solution (50µM). The mixture was firstly stirred in dark environment for 30 minutes to achieve adsorption-desorption equilibrium, and then exposed to natural sunlight for 90 minutes. Aliquots were taken at specific intervals, filtered, and analysed using a UV-vis spectrophotometer. To assess catalyst stability, the used MoS_2 sample was recovered through centrifugation and dried overnight at 60°C. The recovered catalyst underwent five consecutive photocatalytic cycles under identical conditions to evaluate its reusability. For adsorption studies, various experimental parameters were systematically optimized, including catalyst dosage, contact time, initial dye concentration, and solution pH. The adsorption (% C_{ads}) and photocatalytic degradation (% C_{deg}) efficiency of the photocatalyst was calculated using the following equations:

$$\%C_{ads} = \frac{C_{in} - C_0}{C_{in}} \times 100$$

$$\%C_{deg} = \frac{C_0 - C_t}{C_0} \times 100$$

Where, C_{in}, C_0, and C_t represent the concentrations of MB dye at the initial stage, after reaching adsorption–desorption equilibrium, and at time t, respectively.

Additionally, the photocatalytic mechanism was investigated through radical trapping experiments using specific scavengers: EDTA-2Na for holes (h^+), benzoquinone (BQ) for superoxide radicals ($\bullet O_2^-$), $AgNO_3$ for electrons (e^-) and isopropyl alcohol (IPA) for hydroxyl radicals (•OH). The radical trapping experiments were conducted following the same protocol as the degradation studies, with 1 mM of each scavenger added to the MB solution before introducing the catalyst.

2 Lists of Figures and Tables

2.1 TEM-EDS

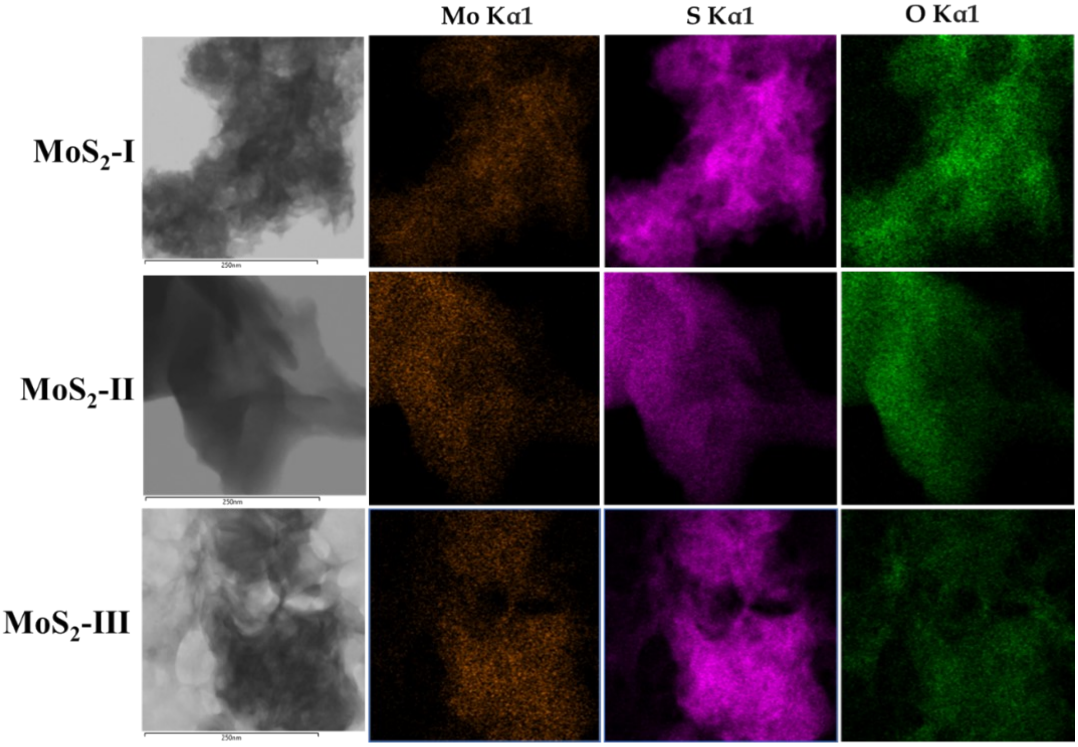

Figure S1. TEM-EDS mapping of MoS_2 samples.

2.2 XPS spectra

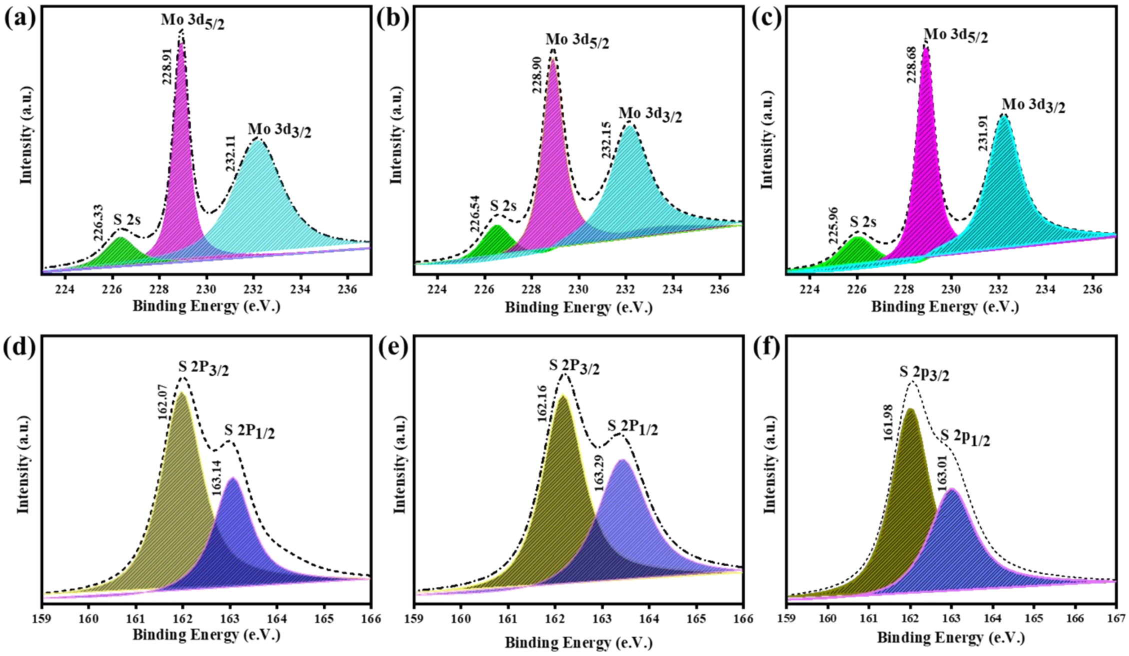

Figure S2. XPS spectra showing Mo 3d **(a-c)** and S 2p **(d-f)** regions for MoS_2-I, MoS_2-II, and MoS_2-III, respectively.

The high-resolution XPS spectra of all MoS_2 samples showed characteristic peaks for both Mo and S.[1] as shown in **Figure S2(a-c)**. MoS_2-I showed peaks at 228.91 and 232.11 eV, MoS_2-II at 228.90 and 232.15 eV, and MoS_2-III at 228.68 and 231.91 eV, corresponding to Mo^{4+} $3d_{5/2}$ and Mo^{4+} $3d_{3/2}$ states, respectively. The slight shift to lower binding energy observed in MoS_2-III indicates the presence of mixed-phase MoS_2, also consistent with reported binding energy difference of 0.5-0.9 eV between 2H and 1T phases.[2,3] Additional S 2s peaks were observed at 226.33 eV (MoS_2-I), 226.54 eV (MoS_2-II), and 225.96 eV (MoS_2-III). The S 2p spectra exhibited two main peaks corresponding to S $2p_{3/2}$ and S $2p_{1/2}$ orbitals, shown in **Figure S2(d-f)**. These peaks were observed at 161.965 and 163.04 eV for MoS_2-I, 162.16 and 163.29 eV for MoS_2-II, and 161.88 and 163.01 eV for MoS_2-III, aligning closely with previous studies.[4] Thus, these spectral features indicate the formation of pure 2H phase in both MoS_2-I and MoS_2-II samples and a mixed 1T/2H phase in MoS_2-III.

2.3 FTIR Spectra

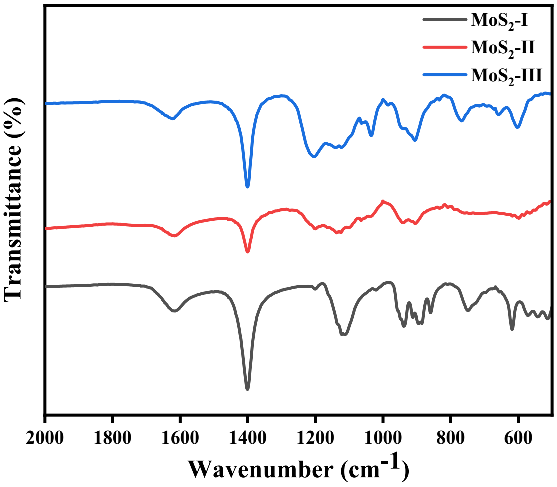

Figure S3. FTIR spectra of MoS$_2$ samples.

2.4 BET and TGA

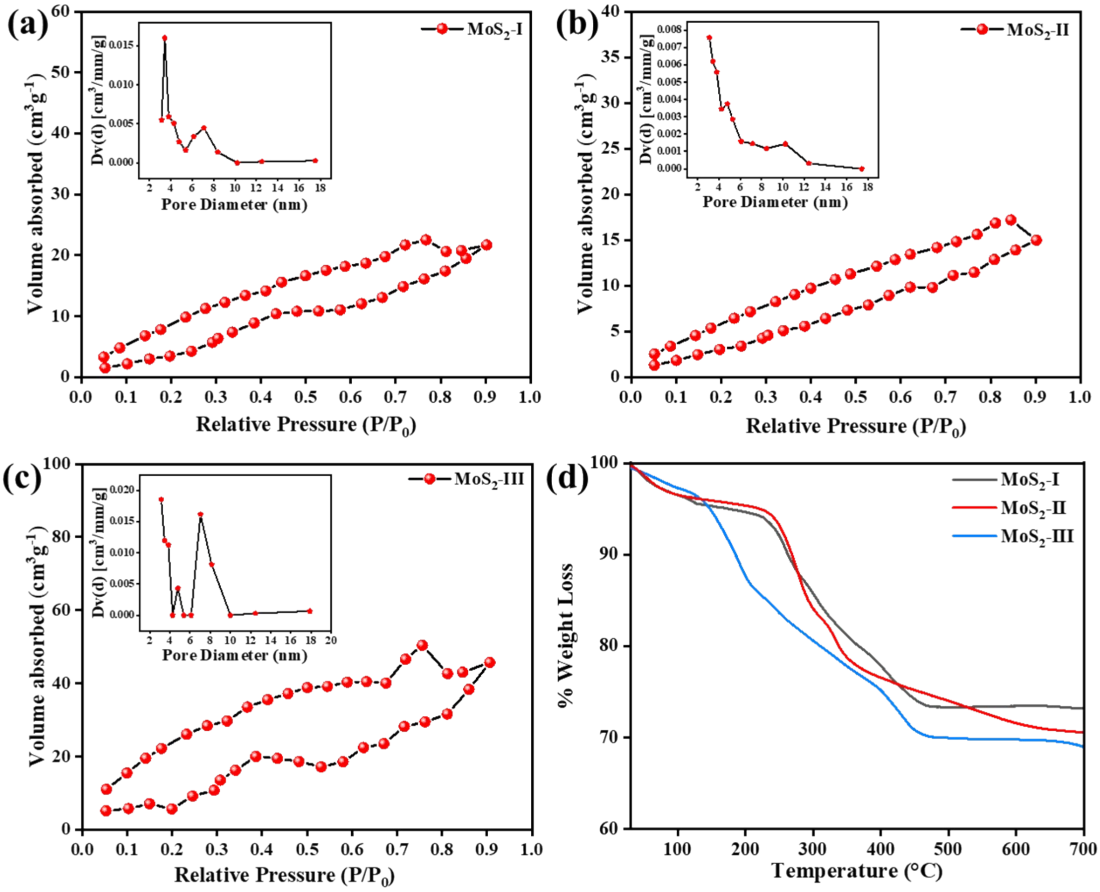

Figure.S4 (a-c) N_2 adsorption-desorption isotherms with BJH pore size distribution (shown in inset) of MoS_2 samples. **(d)** Thermal decomposition profiles obtained from TGA analysis of MoS_2 samples.

The specific surface area and porosity of MoS_2 samples were examined using the N_2 adsorption-desorption method, which revealed a type IV isotherm pattern with H3 hysteresis loop (**Figure S4(a-c)**) indicating a mesoporous structure originated from the interstitial spaces created by the interconnected network of MoS_2 nanosheets. Using the multipoint BET method, the specific surface areas were determined to be 26.1, 17.5, and 40.5 m^2/g for MoS_2-I, MoS_2-II, and MoS_2-III samples, respectively. The corresponding pore size distribution, calculated from the desorption branch of the nitrogen isotherm (**Figure S4(a-c), inset**), showed a relatively broad range of mesopores. This relatively large surface area and porosity (listed in **Table S1)** can provide more active sites for the adsorption of pollutant molecules, which is beneficial for the rapid adsorption and transfer of adsorbates within the hierarchically porous structure. The TGA curves for MoS_2 samples revealed distinct weight loss patterns across the temperature range up to 700°C, as shown in **Figure S4(d)**. The initial weight loss up to 120°C, was corresponding to the evaporation of surface-adsorbed water molecules. The weight loss observed near 300°C, attributed to the oxidation of MoS_2 to MoO_3 and the decomposition of residual precursor materials.[5] The total thermal decomposition process resulted in total weight losses of 26.94%, 29.32%, and 31.03% for MoS_2-I, MoS_2-II, and MoS_2-III samples, respectively. These moderate weight loss values across the elevated temperature range demonstrate the robust thermal stability of all synthesized MoS_2 samples.

Table S1. Surface area and Pore characteristics of MoS_2 samples determined by BET analysis.

Sample	**Surface area (m^2 g^{-1})**	**Pore size (nm)**	**Pore volume (cm^3 g^{-1})**
MoS_2-I	26.1	3.4	0.03
MoS_2-II	17.5	3.1	0.02
MoS_2-III	40.5	3.2	0.05

2.5 Tauc plots

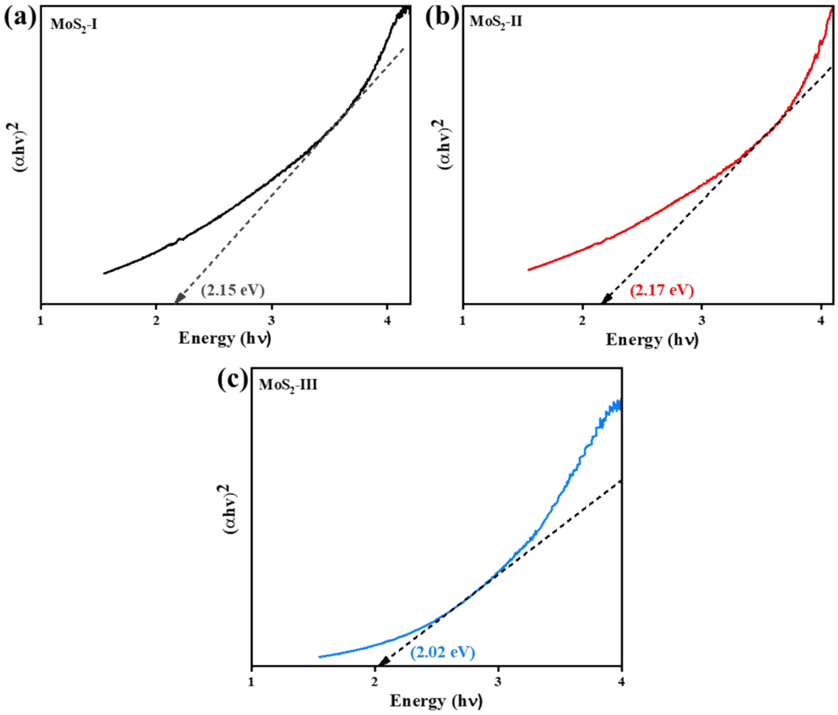

Figure S5. Tauc plots of MoS_2 samples**.**

Bandgap analysis using Tauc plots revealed varying energy gaps among the synthesized samples: 2.15 eV for MoS_2-I, 2.17 eV for MoS_2-II, and 2.02 eV for MoS_2-III. The notably lower bandgap observed in MoS_2-III can be attributed to the incorporation of the 1T phase within its structure.

2.6 Photocatalytic Degradation of MB dye by MoS_2 Photocatalysts across three experimental batches

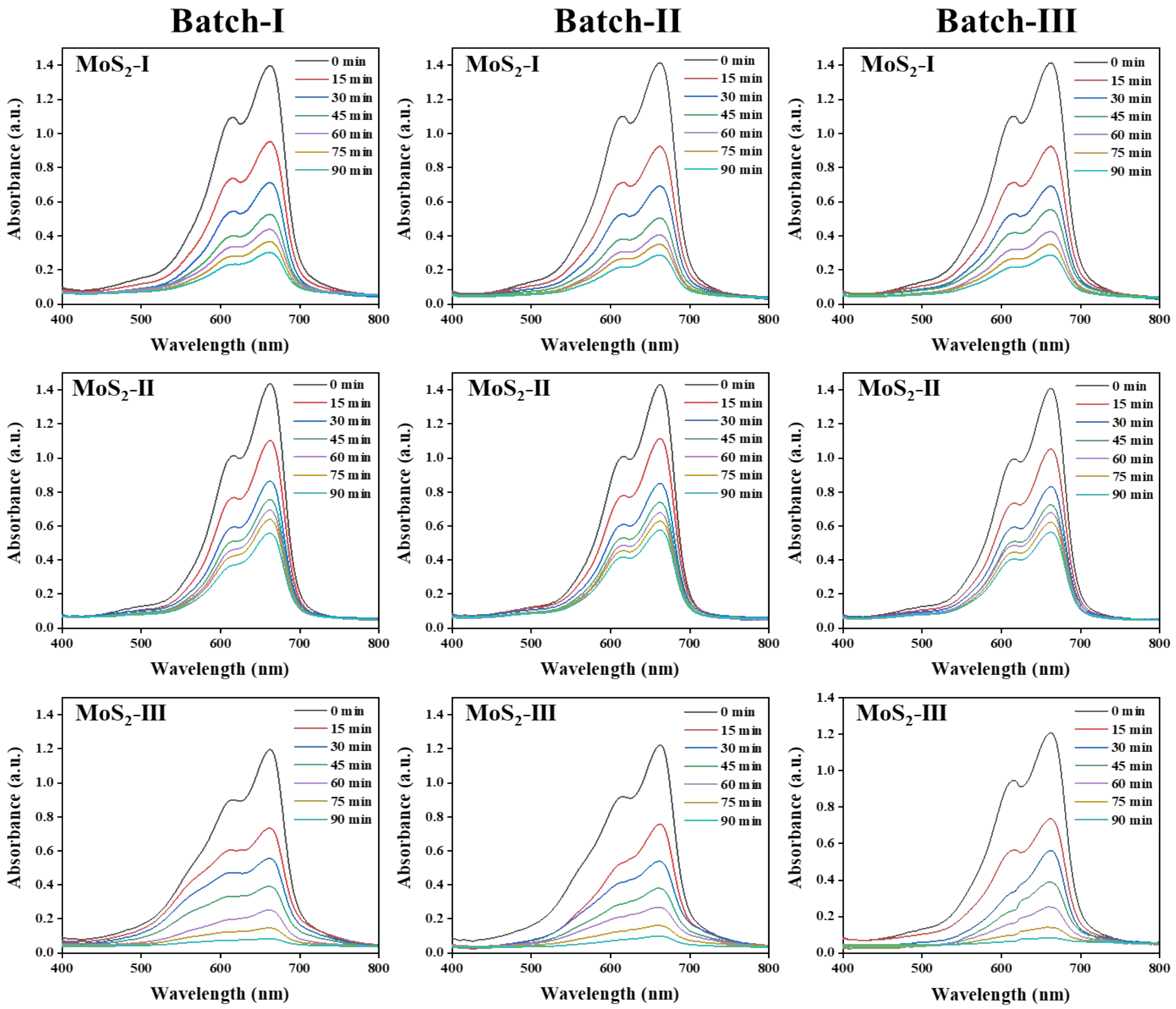

Figure S6. UV-visible absorption spectra showing the photocatalytic degradation of MB dye using MoS_2-I, MoS_2-II, and MoS_2-III across three experimental batches.

2.7 Calibration curve for MB dye

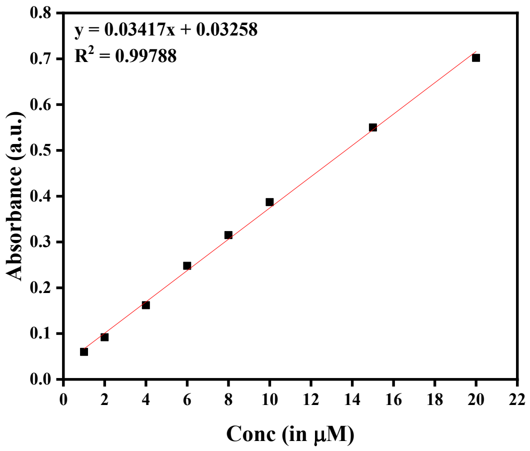

Figure S7. Standard curve for MB dye demonstrates various dye concentrations, including the equation and R-squared value.

2.8 Effect of various parameters on adsorption capacity of MoS_2-III

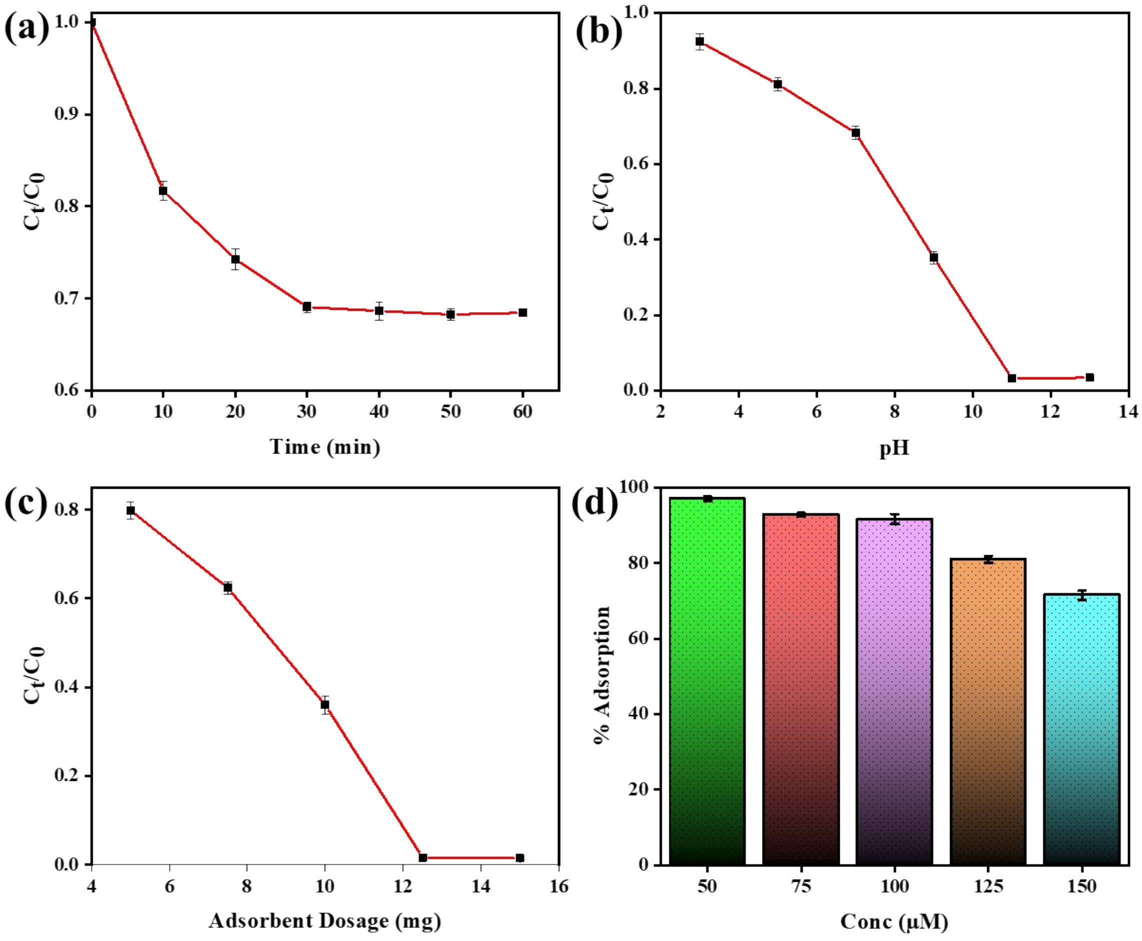

Figure S8. Adsorption performance of MoS_2-III for MB dye removal: effect of **(a)** contact time, **(b)** solution pH, **(c)** adsorbent dosage, and **(d)** initial dye concentration.

Effect of contact time. The adsorption behaviour was studied using 10 mg MoS_2-III with 50 ml of 50 µM MB solution over 60 minutes. As shown in **Figure S8(a)**, the adsorption capacity showed rapid initial increase due to abundant active sites, gradually reaching equilibrium at 30 minutes. This efficient adsorption suggests MoS_2 as high-performance adsorbent due to its electrostatic attraction and π-π stacking interactions with MB molecules.[6]

Effect of pH. The pH-dependent adsorption behaviour of MoS_2-III was investigated at pH values ranging from 3 to 13 at room temperature for 30 minutes. The results, illustrated in **Figure S8(b)**, revealed a strong correlation between pH and removal efficiency, with the adsorption rate dramatically improving under basic conditions. Specifically, the removal efficiency increased more than tenfold, from 9% at pH 3 to 97% at pH 11 This behaviour is consistent with the cationic nature of MB dye, which favours basic environments.[7] At lower pH, H^+ ions compete with dye molecules for adsorption sites, while higher pH increases surface charge density, enhancing electrostatic attractions between dye and MoS_2 surface.[6]

Effect of adsorbent dosage. MoS_2-III dosage was varied from 5-15 mg at constant MB concentration (shown in **Figure S8(c)**). Higher adsorbent amounts improved MB removal efficiency due to increased adsorption sites. However, beyond 12.5 mg, the removal efficiency of MB in the solution by the adsorbent did not substantially increase, indicating underutilization of active sites at higher dosages.[8]

Effect of initial dye concentration. The concentration dependence adsorption behaviour was examined using 50 mL MB solutions ranging from 50 to 150 µM with 12.5 mg MoS_2 at pH 11 for the optimal contact time of 30 minutes. **Figure S8(d)** shows that the removal efficiency decreased from 95.8 ± 0.8 % to 69.9 ± 1.7 % as initial concentration increased from 50 to 150 µM. This inverse relationship between removal efficiency and initial concentration indicates a finite number of active sites available on the MoS_2 surface for dye adsorption.

Table S2. Adsorption isotherm models along with their linear equations used in the present study.

Isotherm Model	Plot	Linear Equation	References
Langmuir	$C_e/q_e \text{ vs. } C_e$	$\frac{C_e}{q} = \frac{1}{Q_m b} + \frac{C_e}{Q_m}$	9
Freundlich	$ln q_e \text{ vs. } lnC_e$	$lnq = \frac{lnC_e}{n} + lnK_f$	10
Temkin	$q_e \text{ vs. } lnC_e$	$q = BlnK_t + BlnC_e$	11

In these isotherm models, q represents the equilibrium adsorption capacity, C_e is the equilibrium concentration, b is the Langmuir constant and Q_m denotes the maximum adsorption capacity. For the Freundlich model, K_f and 1/n represent the adsorption capacity and intensity constants, respectively. In the Temkin model, B and K_t are Temkin constants.

2.9 Adsorption isotherm plots

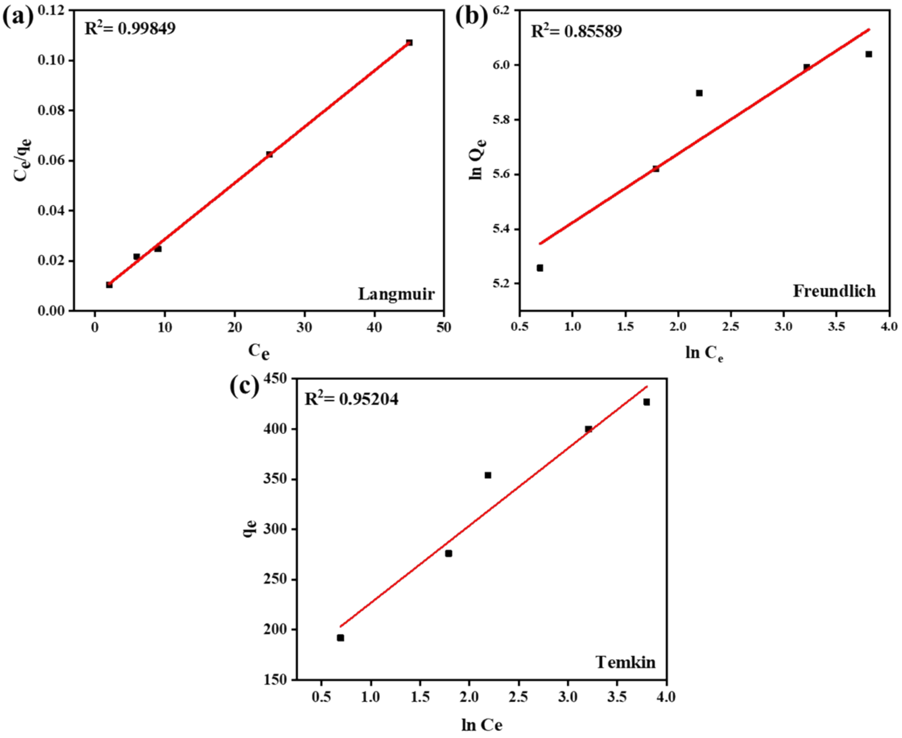

Figure S9. Adsorption isotherms of MoS_2-III fitted to **(a)** Langmuir, **(b)** Freundlich, and **(c)** Temkin isotherm.

Table S3. Comparison between MoS_2 and other adsorbents used for the adsorption of MB dye.

Adsorbent	**Q_m**	**Ref**
MoS_2 nanostructure	208 mg/g	[7]
MoS_2 nanoflowers	200 mg/g	[12]
MoS_2 nanosheet	95.31 mg/g	[13]
MoS_2 ultrathin nanosheets	146.43 mg/g	[6]
MoS_2 nanosheet	297 mg/g	[14]
Graphene oxide	454.54 mg/g	[8]
Mesoporous activated carbon	364.2 mg/g	[15]
$ZnCl_2$-activated carbon	156.25 mg/g	[16]
Mesoporous activated carbon	195.2 mg/g	[17]
MoS_2 nanosheets	446.42 mg/g	**Present study**

2.10 Kinetics of MB dye degradation

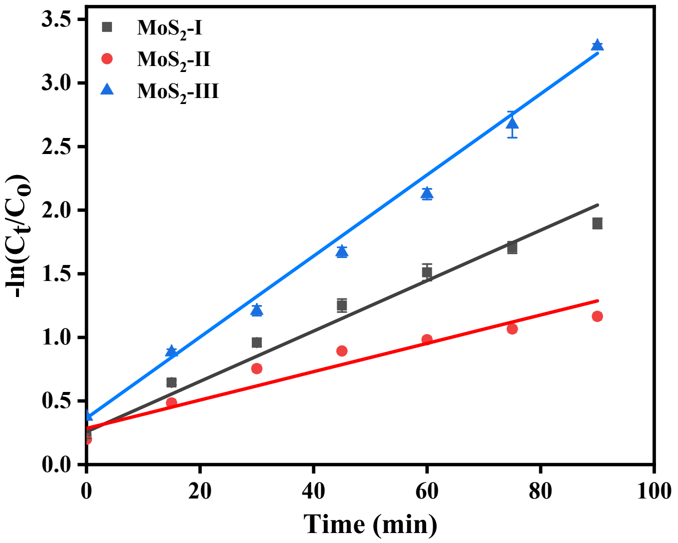

Figure S10. Pseudo-first-order kinetics plots of MoS_2 samples.

Table S4. Comparing the MB dye degradation performance of prepared MoS_2 samples with similar 2D photocatalysts

Photocatalyst	**Catalyst dosage (mg.L^{-1})**	**MB concentration (µM)**	**Light source**	**Time (in min)**	**Removal efficiency (%)**	**Ref**
GO	200	50	Sunlight	120	99	[8]
GO	200	20	Sunlight	120	91	[18]
rGO	400	45	Visible	100	66	[19]
Water soluble Graphene	200	50	Visible	90	96%	[20]
MoS_2	200	60	Visible	120	98	[21]
1T/2H-MoS_2	100	15	Visible	180	80	[22]
$Ti_3C_2T_x$ (MXene)	100	31	Sunlight	120	10	[23]
MoS_2-rGO	1000	188	Visible	60	99%	[24]
MoS_2-III	200	50	Sunlight	90	97.84%	**This work**

2.11 Recyclability study

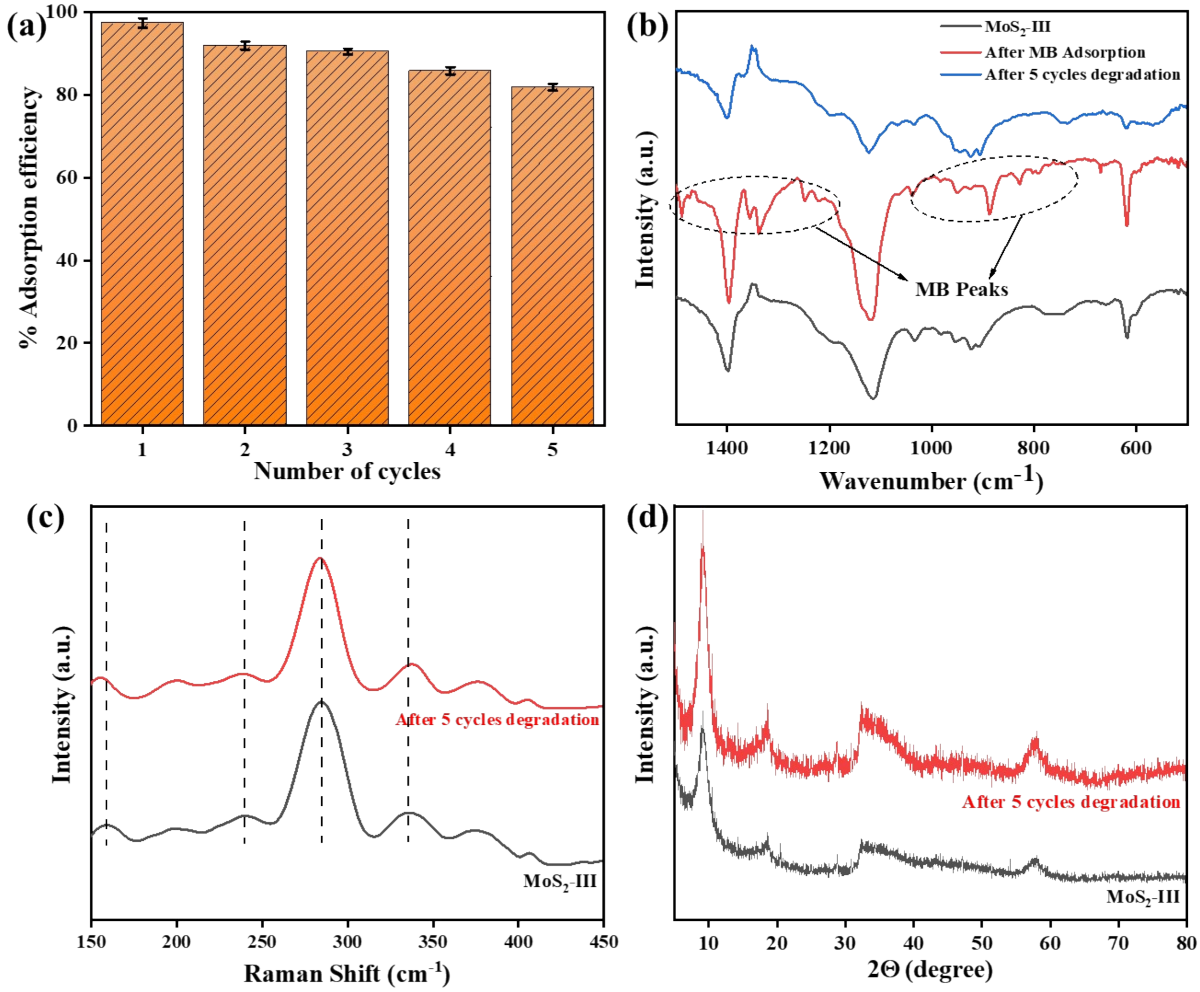

Figure S11. (a) Dye removal efficiency of MoS$_2$-III after recovery. **(b)** FTIR spectra after adsorption and photodegradation of MB by MoS$_2$-III. **(c)** Raman spectra and **(d)** XRD patterns of pristine MoS$_2$-III and the photocatalyst obtained after 5 degradation cycles.

The appearance of additional peaks in the FTIR spectra (e.g., 1489 cm^{-1} for C=C side ring stretching, 1330-1360 cm^{-1} for -CH$_2$ or -CH$_3$ stretching, 1250 cm^{-1} for -C-N, 1048 cm^{-1} for C-S-C, 881 and 824 cm^{-1} for C-H out of plane bending etc. of MoS$_2$-III sample after the adsorption of MB dye confirms the stacking of dye molecules onto the surface of MoS$_2$.[25]

3. References

1 Z. Wu, D. Wang and A. Sun, *J Mater Sci*, 2010, **45**, 182–187.

2 Y. Qi, Q. Xu, Y. Wang, B. Yan, Y. Ren and Z. Chen, *ACS Nano*, 2016, **10**, 2903–2909.

3 S. Shi, Z. Sun and Y. H. Hu, *Journal of Materials Chemistry A*, 2018, **6**, 23932–23977.

4 R. Zhang, Y. Li, J. Qi and D. Gao, *Nanoscale Res Lett*, 2014, **9**, 586.

5 A. Bahuguna, S. Kumar, V. Sharma, K. L. Reddy, K. Bhattacharyya, P. C. Ravikumar and V. Krishnan, *ACS Sustainable Chem. Eng.*, 2017, **5**, 8551–8567.

6 X.-Q. Qiao, F.-C. Hu, F.-Y. Tian, D.-F. Hou and D.-S. Li, *Rsc Advances*, 2016, **6**, 11631–11636.

7 S. Han, K. Liu, L. Hu, F. Teng, P. Yu and Y. Zhu, *Sci Rep*, 2017, **7**, 43599.

8 S. Thakur, A. Badoni, Samriti, P. Sharma, A. Ojha, H. C. Swart, A. Y. Kuznetsov and J. Prakash, *Langmuir*, 2024, **40**, 18486–18502.

9 I. Langmuir, *J. Am. Chem. Soc.*, 1918, **40**, 1361–1403.

10 H. Freundlich, *Zeitschrift für Physikalische Chemie*, 1907, **57U**, 385–470.

11 M. Vadi, A. O. Mansoorabad, M. Mohammadi and N. Rostami, *Asian Journal of Chemistry*, 2013, **25**, 5467.

12 X. Wang, P. Zhang, F. Xu, B. Sun, G. Hong and L. Bao, *Sustainability*, 2022, **14**, 7585.

13 C. Zhang, X. Li, C. Lian, C. Hu, S. Duo and Q. Hu, *Journal of Nanoscience and Nanotechnology*, 2018, **18**, 7948–7951.

14 A. T. Massey, R. Gusain, S. Kumari and O. P. Khatri, *Ind. Eng. Chem. Res.*, 2016, **55**, 7124–7131.

15 A. S. Abdulhameed, N. N. M. Firdaus Hum, S. Rangabhashiyam, A. H. Jawad, L. D. Wilson, Z. M. Yaseen, A. A. Al-Kahtani and Z. A. ALOthman, *Journal of Environmental Chemical Engineering*, 2021, **9**, 105530.

16 H. K. Yağmur and İ. Kaya, *Journal of Molecular Structure*, 2021, **1232**, 130071.

17 A. H. Jawad, A. Saud Abdulhameed, L. D. Wilson, S. S. A. Syed-Hassan, Z. A. ALOthman and M. Rizwan Khan, *Chinese Journal of Chemical Engineering*, 2021, **32**, 281–290.

18 Samriti, S. Thakur, A. Ojha, R. Gupta, M. Bechelany, A. Yu. Kuznetsov, H. C. Swart and J. Prakash, *Physica Status Solidi (a)*, 2024, 2400169.

19 A. Negash, S. Mohammed, H. D. Weldekirstos, A. D. Ambaye and M. Gashu, *Scientific Reports*, 2023, **13**, 22234.

20 A. Singh, P. Khare, S. Verma, A. Bhati, A. K. Sonker, K. M. Tripathi and S. K. Sonkar, *ACS Sustainable Chem. Eng.*, 2017, **5**, 8860–8869.

21 M. T. Leng Lai, K. Mun Lee, T. C. Kuang Yang, G. Ting Pan, C. Wei Lai, C.-Y. Chen, M. Rafie Johan and J. Ching Juan, *Nanoscale Advances*, 2021, **3**, 1106–1120.

22 D. Mouloua, M. Lejeune, N. S. Rajput, K. Kaja, M. El Marssi, M. A. El Khakani and M. Jouiad, *Ultrasonics Sonochemistry*, 2023, **95**, 106381.

23 Z. Othman, A. Sinopoli, H. R. Mackey and K. A. Mahmoud, *ACS Omega*, 2021, **6**, 33325–33338.

24 J. Li, X. Liu, L. Pan, W. Qin, T. Chen and Z. Sun, *RSC Adv.*, 2014, **4**, 9647–9651.

25 A. Gopalakrishnan, S. P. Singh and S. Badhulika, *New Journal of Chemistry*, 2020, **44**, 5489–5500.